

Quark number densities at imaginary chemical potential in $N_f = 2$ lattice QCD with Wilson fermions and its model analyses

Junichi Takahashi,^{1,*} Hiroaki Kouno,^{2,†} and Masanobu Yahiro^{1,‡}

¹*Department of Physics, Graduate School of Sciences, Kyushu University, Fukuoka 812-8581, Japan*

²*Department of Physics, Saga University, Saga 840-8502, Japan*

(Dated: June 9, 2019)

We investigate the chemical-potential (μ) dependence of quark number densities (n_q) at both imaginary and real μ by using $N_f = 2$ lattice QCD and the hadron resonance gas (HRG) model. Quark number densities are first calculated at imaginary μ with lattice QCD on an $8^2 \times 16 \times 4$ lattice with the clover-improved $N_f = 2$ Wilson fermion action and the renormalization-group-improved Iwasaki gauge action. The present results are consistent with the previous results of the staggered-type quark action. The n_q thus obtained are extrapolated to real μ by assuming the Fourier series for the confinement region and the polynomial series for the deconfinement region. The extrapolated results are also consistent with the previous results of the Taylor expansion method for the reweighting factor. The upper bound $(\mu/T)_{\max}$ of the reliable extrapolation is estimated for each temperature T . We deduce nucleon and Δ -resonance masses in the vicinity of the pseudocritical temperature (T_c) with the HRG model from LQCD data on n_q at imaginary μ . The resulting nucleon and Δ -resonance masses reduce by about 10% as T increases from $T = 0.93T_c$ to $0.99T_c$.

PACS numbers: 11.15.Ha, 12.38.Gc, 11.30.Fs

I. INTRODUCTION

There are many interesting topics on quantum chromodynamics (QCD) at high density. The observation [1] of a two-solar-mass neutron star has an impact on the equation of state (EoS) of dense matter and the QCD phase diagram at high density. The experiments of relativistic heavy-ion collisions, for example the Beam Energy Scan experiments, are exploring QCD not only at finite temperature T but also at finite quark-chemical potential μ [2, 3]. Lattice QCD (LQCD) is the first-principle calculation to study QCD, but has the serious sign problem at finite μ .

In LQCD, the fermion determinant $\det M(\mu/T)$ becomes complex for finite real μ , because

$$(\det M(\mu/T))^* = \det M(-\mu^*/T) = \det M(-\mu/T). \quad (1)$$

This interferes with the use of Monte-Carlo simulations based on the importance sampling. For this reason, several methods were proposed so far in order to avoid the sign problem [4, 5]. Very recently, the complex Langevin method [6–9] and the Lefschetz thimble theory [10, 11] have attracted much attention as the method to go beyond $\mu/T = 1$.

One of the methods to avoid the sign problem is the imaginary- μ approach. For pure imaginary chemical potential $\mu = i\mu_I$, it is convenient to introduce the dimensionless chemical potential $\theta = \mu_I/T$. The first equality of Eq. (1) shows that the fermion determinant $\det M(i\theta)$ is real for imaginary μ . This makes LQCD simulations feasible there. Observables at real μ are extracted from those at imaginary μ by assuming functional forms for the observables.

In the imaginary μ region, QCD has two characteristic properties: One is the Roberge-Weiss (RW) periodicity and the other is the RW phase transition [12]. Figure 1 shows a schematic graph for the QCD phase diagram in the T - θ plane. The QCD grand partition function $Z(\theta)$ has a periodicity of $2\pi/N_c$ in θ :

$$Z(\theta) = Z\left(\theta + \frac{2\pi k}{N_c}\right), \quad (2)$$

where N_c is the number of colors and $k = 1, \dots, N_c$. This is a remnant of \mathbb{Z}_{N_c} symmetry in pure gauge theory and is now called the RW periodicity. Meanwhile, the RW transition is the first-order phase transition appearing at T higher than some temperature T_{RW} and $\theta = \pi/N_c$. This transition line and its \mathbb{Z}_{N_c} images are plotted by the solid lines in Fig. 1, whereas the confinement/deconfinement crossover is drawn by the dashed lines. The point located at $(T, \theta) = (T_{\text{RW}}, \pi/N_c)$ is called the RW endpoint. The critical temperature T_{RW} is larger than the pseudocritical temperature T_c of the deconfinement crossover at zero μ [13]; T_{RW} is located between $1.08T_c$ and $1.20T_c$, as shown later. The order parameter of the RW transition is a \mathcal{C} -odd quantity such as the phase of the Polyakov loop or the quark-number density [14], where \mathcal{C} means charge conjugation. The existence of the RW transition and the RW periodicity is numerically confirmed with LQCD simulations [15–20] and the underlying mechanism is clearly understood with the effective model [14, 21, 22] by introducing a new concept of extended \mathbb{Z}_{N_c} symmetry.

The quark number density n_q is a fundamental quantity to study high-density physics and important in determining the EoS at finite real μ . The EoS plays an essential role in investigating the structure of neutron stars. Moreover, n_q is useful to determine the strength of vector-type interaction in the effective model [23, 24]. For small real μ/T , the quark number density was calculated with the Taylor expansion method for the reweighting factor in which either the staggered-type [25] or the Wilson-type quark action [26] is

*takahashi@phys.kyushu-u.ac.jp

†kounoh@cc.saga-u.ac.jp

‡yahiro@phys.kyushu-u.ac.jp

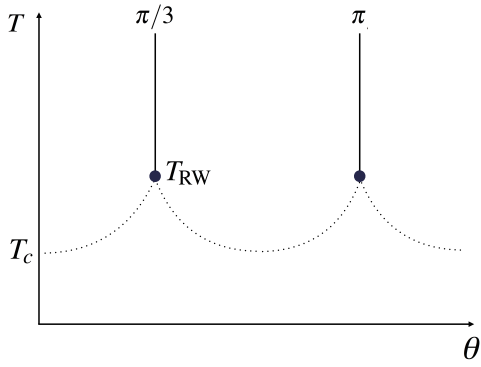


Fig. 1: QCD phase diagram in the imaginary μ region. The solid and dashed lines stand for the RW phase transition and the deconfinement crossover, respectively.

taken. The quark number density is also computed at imaginary μ in Refs. [17, 18, 27, 28] with the staggered-type quark action, and n_q at real μ is deduced from that at imaginary μ by assuming analytic forms for n_q .

In this paper, we investigate the μ dependence of n_q at both imaginary and real μ . We first perform LQCD simulations at imaginary μ with the Wilson-type quark action, since the quark number density was never calculated with the Wilson-type quark action at imaginary μ . LQCD simulations at imaginary μ do not require any special prescription in numerical calculations, since there is no sign problem there. The n_q thus obtained at imaginary μ are extrapolated to the real μ region by assuming functional forms for n_q . This analytic-continuation is confirmed to be reliable by comparing the extrapolated results with the previous results [26] based on the Taylor expansion method for the reweighting factor. The upper bound $(\mu/T)_{\max}$ of the reliable extrapolation is estimated for each T .

The hadron resonance gas (HRG) model is reliable in the confinement region. For the the 2+1 flavor case with no μ , in fact, it is shown that the model well reproduces LQCD data on pressure at $T < 1.2T_c$ [29]. As shown in Fig. 1, the pseudocritical temperature of deconfinement transition goes down from $T = T_{RW}$ to T_c as $(\mu/T)^2$ increases from $-(\pi/N_c)^2$. When we are interested in the vicinity of T_c , the HRG model is more reliable at imaginary μ than at real μ . Using this property, we deduce the T dependence of nucleon and Δ -resonance masses in the vicinity of T_c with the HRG model from LQCD data on n_q at imaginary μ .

Actual LQCD simulations are done on an $8^2 \times 16 \times 4$ lattice with the clover-improved two-flavor Wilson fermion action and the renormalization-group-improved Iwasaki gauge action. We consider two temperatures $T/T_c = 0.93$ and 0.99 in the confinement region and four temperatures $T/T_c = 1.08, 1.20, 1.35$ and 2.07 in the deconfinement region. Following the previous LQCD simulation [26], we compute n_q along the line of constant physics at $m_{PS}/m_V = 0.80$, where

m_{PS} and m_V are pseudoscalar- and vector-meson masses, respectively. This corresponds to the case of the pion mass $m_\pi \sim 616$ MeV and the quark mass $m_q \sim 130$ MeV [24] for $T_c \sim 171$ MeV [30]. The analytic continuation is carried out with the Fourier series for $T < T_c$ and the polynomial series for $T > T_{RW}$.

This paper is organized as follows. In Sec. II, we explain the lattice action, the quark number density and the analytic continuation. In Sec. III, we show our simulation parameters and numerical results for n_q at both imaginary and real μ . In Sec. IV, we deduce nucleon and Δ -resonance masses from n_q at imaginary μ by using the HRG model. Section V is devoted to a summary.

II. FORMULATION

A. Lattice action

We use the renormalization-group-improved Iwasaki gauge action S_g [31] and the clover-improved two-flavor Wilson quark action S_q [32] defined by

$$S = S_g + S_q, \quad (3)$$

$$S_g = -\beta \sum_x \left(c_0 \sum_{\mu < \nu; \mu, \nu = 1}^4 W_{\mu\nu}^{1 \times 1}(x) + c_1 \sum_{\mu \neq \nu; \mu, \nu = 1}^4 W_{\mu\nu}^{1 \times 2}(x) \right), \quad (4)$$

$$S_q = \sum_{f=u,d} \sum_{x,y} \bar{\psi}_x^f M_{x,y} \psi_y^f, \quad (5)$$

where $\beta = 6/g^2$ for the gauge coupling g , $c_1 = -0.331$, $c_0 = 1 - 8c_1$, and

$$M_{x,y} = \delta_{xy} - \kappa \sum_{i=1}^3 \{ (1 - \gamma_i) U_{x,i} \delta_{x+\hat{i},y} + (1 + \gamma_i) U_{y,i}^\dagger \delta_{x,y+\hat{i}} \} - \kappa \{ e^{\hat{\mu}} (1 - \gamma_4) U_{x,4} \delta_{x+\hat{4},y} + e^{-\hat{\mu}} (1 + \gamma_4) U_{y,4}^\dagger \delta_{x,y+\hat{4}} \} - \delta_{xy} c_{SW} \kappa \sum_{\mu < \nu} \sigma_{\mu\nu} F_{\mu\nu}. \quad (6)$$

Here κ is the hopping parameter, $\hat{\mu}$ is the quark chemical potential in lattice units, and the lattice field strength $F_{\mu\nu}$ is defined as $F_{\mu\nu} = (f_{\mu\nu} - f_{\mu\nu}^\dagger)/(8i)$ with $f_{\mu\nu}$ the standard clover-shaped combination of gauge links. For the clover coefficient c_{SW} , we take the mean-field value estimated from $W^{1 \times 1}$ in the one-loop level: $c_{SW} = (W^{1 \times 1})^{-3/4} = (1 - 0.8412\beta^{-1})^{-3/4}$ [31]. The value of κ is determined at $\mu = 0$ for each β along the line of constant physics with $m_{PS}/m_V = 0.80$ [30, 33, 34].

B. Quark number density

The quark number density n_q is defined as

$$\frac{n_q}{T^3} = \frac{1}{VT^2} \frac{\partial}{\partial \mu} \ln Z \quad (7)$$

$$= \frac{N_f N_t^3}{N_V} \text{tr} \left[M^{-1} \frac{\partial M}{\partial \mu} \right], \quad (8)$$

where V is the volume, N_f is the number of flavors, N_t is the temporal lattice size, N_V is the lattice volume and M is the fermion matrix. We apply the random-noise method for the trace in Eq. (8). The number of noise vectors is about 4,000. The partition function Z is μ -even (\mathcal{C} -even), so that n_q is μ -odd (\mathcal{C} -odd) from Eq. (7). This means that n_q is pure imaginary for imaginary μ ; actually,

$$n_q^* = \left(\frac{1}{V} \frac{\partial \ln Z}{\partial (i\theta)} \right)^* = \frac{1}{V} \frac{\partial \ln Z}{\partial (-i\theta)} = -n_q. \quad (9)$$

We have confirmed in our LQCD simulations that the real part of n_q is zero at imaginary μ . For later convenience, we represent the imaginary part of n_q by n_q^I : $n_q^I = \text{Im}(n_q)$.

C. Analytic continuation

Our final interest is n_q at real μ . We then extrapolate the n_q calculated at imaginary μ with LQCD to the real μ region, assuming some functional forms for n_q .

In the imaginary- μ region, n_q is a θ -odd function with the RW periodicity. We then consider only a period $-\pi/3 < \theta \leq \pi/3$ for simplicity. In the confinement region at $T < T_c$, the quark number density is smooth for any θ , indicating that $n_q = 0$ at $\theta = 0, \pm\pi/3$ [14, 21, 22]. Hence n_q can be described with good accuracy by a partial sum $S_F^n(T, \theta)$ of the Fourier series:

$$\frac{n_q(T, i\theta)}{T^3} \approx i S_F^n(T, \theta) = i \sum_{k=1}^n a_F^{(k)}(T) \sin(3k\theta) \quad (10)$$

where the superscript n of $S_F^n(T, \theta)$ represents the highest order in the partial sum. The coefficients $a_F^{(k)}(T)$ are obtained by fitting the function (10) to LQCD data at imaginary $\mu = i\mu_I$. The analytic continuation from $\mu = i\mu_I$ to $\mu = \mu_R$ can be made by replacing $i\mu_I/T$ by μ_R/T in Eq. (10):

$$\begin{aligned} \frac{n_q(T, \mu_R/T)}{T^3} &\approx g_F^n \left(T, \frac{\mu_R}{T} \right) \\ &= \sum_{k=1}^n a_F^{(k)}(T) \sinh \left(3k \frac{\mu_R}{T} \right). \end{aligned} \quad (11)$$

Here note that the coefficients $a_F^{(k)}(T)$ have already been determined at imaginary μ .

In the region $T_c < T < T_{\text{RW}}$, the system is in the deconfinement region for small θ but in the confinement region for large θ near $\pi/3$, as shown in Fig. 1. Because of this property,

the θ dependence of n_q is complicated and makes the analytic continuation difficult. We then do not perform the analytic continuation in this region.

In the deconfinement region at $T > T_{\text{RW}}$, the quark number density is discontinuous at $\theta = \pm\pi/3$ where the first-order RW phase transition takes place; note that n_q is the order parameter of the RW first-order transition [14]. Owing to this property, n_q monotonically increases with θ , as shown later in Fig. 2. This suggests that n_q can be described with good accuracy by a partial sum $S_p^n(T, \theta)$ of the polynomial series:

$$\frac{n_q(T, i\theta)}{T^3} \approx i S_p^n(T, \theta) = i \sum_{k=1}^n a_p^{(2k-1)}(T) \theta^{2k-1}, \quad (12)$$

where the superscript n of $S_p^n(T, \theta)$ represents the highest order in the partial sum. Again, the analytic continuation is made by replacing $i\mu_I/T$ by μ_R/T in Eq. (12):

$$\begin{aligned} \frac{n_q(T, \mu_R/T)}{T^3} &\approx g_p^n \left(T, \frac{\mu_R}{T} \right) \\ &= \sum_{k=1}^n (-1)^{(k-1)} a_p^{(2k-1)}(T) \left(\frac{\mu_R}{T} \right)^{2k-1}. \end{aligned} \quad (13)$$

III. NUMERICAL RESULTS

Full QCD configurations with $N_f = 2$ dynamical quarks were generated with the hybrid Monte-Carlo algorithm on a lattice of $N_x \times N_y \times N_z \times N_t = 8^2 \times 16 \times 4$. The step size of the molecular dynamics is $\delta\tau = 0.02$ and the step number is $N_\tau = 50$. The acceptance ratio is more than 95%. We generated about 32,000 trajectories and removed the first 4,000 trajectories for the thermalization of all the parameters, and measured n_q at every 100 trajectories. The relation of parameters κ and β to the corresponding T/T_c was determined in Refs. [30, 33, 34]; see Table I for the relation.

κ	β	T/T_c
0.141139	1.80	0.93(5)
0.140070	1.85	0.99(5)
0.138817	1.90	1.08(5)
0.137716	1.95	1.20(6)
0.136931	2.00	1.35(7)
0.135010	2.20	2.07(10)

TABLE I: Summary of the simulation parameter sets determined in Refs. [30, 33, 34]. Here, T_c is the pseudocritical temperature of deconfinement transition at $\mu = 0$. In the parameter setting, the lattice spacing a is about $0.14 \sim 0.2$ fm.

A. Quark number density at imaginary μ

Figure 2 shows n_q^I/T^3 as a function of θ for all the temperatures we consider. The LQCD data are plotted by symbols with error bars, although the error bars are quite small. The number density n_q^I should be zero at $\theta = \pi/3$ below T_{RW} but finite above T_{RW} , since n_q^I is the order parameter of the first-order RW phase transition. One can see from the fact that T_{RW} is located between $1.08T_c$ and $1.2T_c$. The quark number density n_q^I/T^3 behaves as the sine function for $T < T_c$, but monotonically increases up to $\theta = \pi/3$ for $T > T_{RW}$. As for $T = 1.08T_c$, the system is in the deconfinement region for $\theta < 0.8$ but in the confinement region for $0.8 < \theta < \pi/3$, since n_q^I/T^3 increases monotonically up to $\theta \sim 0.7$ but decreases to zero for $\theta > 0.8$. This result is consistent with that of the staggered-type fermion in Ref. [28]. The present result is thus independent of the fermion action taken.

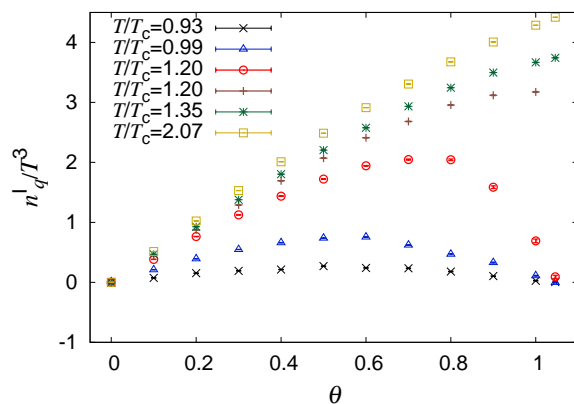


Fig. 2: μ_1/T dependence of n_q^I/T^3 at various values of T . The LQCD data are shown by symbols with error bars, although the error bars are quite small.

First we consider the case of $T < T_c$ and determine the coefficients $a_F^{(k)}(T)$ of the Fourier series from the n_q calculated at imaginary μ with LQCD. In Fig. 3, the results of the χ^2 fittings (curves) are compared with the LQCD results (symbols with error bars). Two cases of S_F^1 and S_F^2 are plotted by dashed and solid curves, respectively. The two results well

reproduce the LQCD data. The coefficients thus obtained are tabulated in Table II together with the χ^2 per degree of freedom (d.o.f). As for $T = 0.93T_c$, the fitting quality is almost same between the two cases of S_F^1 and S_F^2 , as shown by the $\chi^2/\text{d.o.f}$. Furthermore, $a_F^{(2)}$ is much smaller than $a_F^{(1)}$ in the case of S_F^2 . These results show that the coefficients $a_F^{(1)}$ and $a_F^{(2)}$ are determined with high accuracy in the case of S_F^2 . Also for $T = 0.99T_c$, two cases of S_F^1 and S_F^2 are shown in Table II. The deviation of LQCD data from S_F^2 has a θ dependence different from the next-order term $\sin(6\theta)$, so we stopped the χ^2 fitting with S_F^2 .

Next we consider the case of $T > T_{RW}$ and determine the coefficients $a_p^{(2k-1)}(T)$ of the polynomial series. In Fig. 4, the

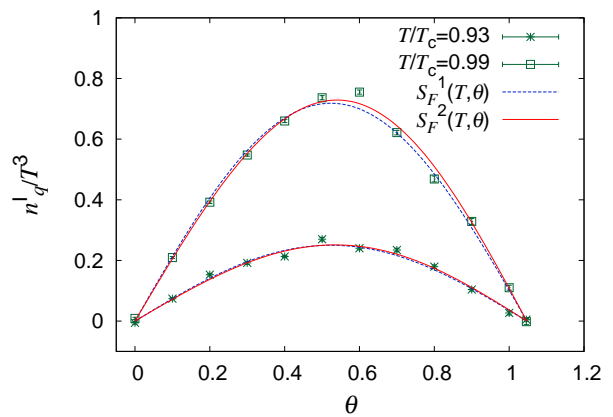


Fig. 3: Results of χ^2 fitting to LQCD data for the case of $T < T_c$. The results of S_F^1 and S_F^2 are plotted by dashed and solid lines, respectively. LQCD data are shown by symbols with error bars.

fitting results (curves) are compared with LQCD data (symbols with error bars) for the case of S_p^3 in panel (a) and for the case of S_p^5 in panel (b). For each temperature, the solid line denotes the χ^2 -minimum result, whereas two dotted lines show the upper and lower bounds of the χ^2 fitting. The resulting coefficients $a_p^{(2k-1)}(T)$ are tabulated in Table III for two cases of S_p^3 and S_p^5 .

T/T_c	$a_F^{(1)}$	$a_F^{(2)}$	$\chi^2/\text{d.o.f}$	μ_1/T (fitting range)
0.93	0.250(2)		5.937	$0 \sim \pi/3$
0.93	0.251(2)	-0.00457(216)	6.084	$0 \sim \pi/3$
0.99	0.718(2)		11.06	$0 \sim \pi/3$
0.99	0.728(3)	-0.0179(26)	7.453	$0 \sim \pi/3$

TABLE II: Coefficients of the Fourier series for S_F^1 and S_F^2 .

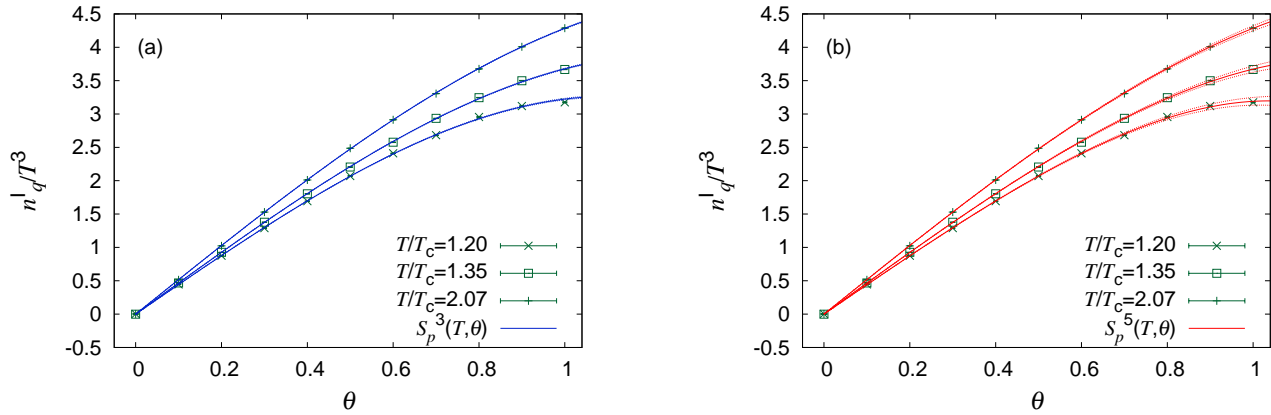


Fig. 4: Results of the χ^2 fitting to LQCD data for the case of $T > T_{RW}$. Panels (a) and (b) show the results of S_p^3 and S_p^5 , respectively. For each temperature, the solid line represents the χ^2 -minimum result, whereas two dotted lines correspond to the upper and lower bounds of the χ^2 fitting. LQCD data are shown by symbols with error bars.

T/T_c	$a_p^{(1)}$	$a_p^{(3)}$	$a_p^{(5)}$	$\chi^2/\text{d.o.f}$	μ_1/T (fitting range)
1.20	4.437(4)	-1.214(7)		13.66	0 ~ 1
1.20	4.407(5)	-1.024(27)	-0.1935(260)	8.472	0 ~ 1
1.35	4.675(3)	-0.9973(49)		6.036	0 ~ 1
1.35	4.662(5)	-0.9223(223)	-0.06736(1956)	5.308	0 ~ 1
2.07	5.174(2)	-0.8904(40)		9.161	0 ~ 1
2.07	5.177(4)	-0.9056(177)	0.01356(1531)	10.21	0 ~ 1

TABLE III: Coefficients of the polynomial series for S_p^3 and S_p^5 .

B. Quark number density at real μ

First we consider the case of $T/T_c < 1$. Figure 5 shows the μ/T dependence of n_q/T^3 for $T = 0.99T_c$. As the extrapolation from imaginary μ to real μ , we consider two cases of g_F^1 and g_F^2 . For each case, the solid line represents the result calculated from the mean value of $a_F^{(k)}$, whereas two dotted lines correspond to the results from the upper and lower bounds of $a_F^{(k)}$. The g_F^2 case has a larger error than the g_F^1 case, because the former error comes from both of $a_F^{(1)}$ and $a_F^{(2)}$ but the latter error does from $a_F^{(1)}$ only. The result of g_F^2 well reproduces the previous LQCD result [26] (symbols with error bars) based on the Taylor expansion method for the reweighting factor in which g_p^3 is assumed for n_q/T^3 but the coefficients $a_p^{(k)}$ are calculated at $\mu = 0$. The previous result thus has contributions up to $(\mu/T)^3$. Meanwhile, the present result of g_F^2 includes the higher-order contributions in addition to contributions up to $(\mu/T)^3$. When the higher-order

contributions are switched off in the result of g_F^2 , we can get the dot-dashed line together with two dotted lines calculated from the upper and lower bounds of $a_F^{(k)}$. The dot-dashed line agrees with the previous result based on the Taylor expansion method for the reweighting factor. The difference between the dot-dashed line and the result of g_F^2 thus represents higher-order corrections to the previous result. From the fact that the difference is small at $\mu/T < 0.9$, we can conclude that both the previous result based on the Taylor expansion method for the reweighting factor and the present result of g_F^2 are reliable at $\mu/T < 0.9$.

Figure 6 shows the μ/T dependence of n_q/T^3 at $T = 0.93T_c$. The definition of lines is the same as in Fig. 5. The difference between two results of g_F^1 and g_F^2 reduces as T decreases from $0.99T_c$ to $0.93T_c$. The extrapolation of g_F^1 and g_F^2 thus becomes more reliable as T decreases. As mentioned above, the g_F^2 extrapolation is reliable at $T = 0.99T_c$ in the range $\mu/T < 0.9$. This means that the g_F^2 extrapolation is reliable also at $T = 0.93T_c$ at least in the range $\mu/T < 0.9$.

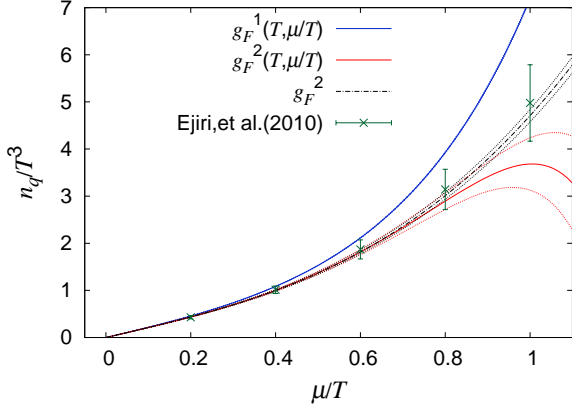


Fig. 5: μ/T dependence of n_q/T^3 at $T = 0.99T_c$. Two cases of g_F^1 and g_F^2 are plotted. For each case, the solid line stands for the result calculated from the mean value of $a_F^{(k)}$, whereas two dashed lines denote the results from the upper and lower bounds of $a_F^{(k)}$. In the dot-dashed line, high-order contributions than $(\mu/T)^3$ are switched off in g_F^2 . The symbols denotes LQCD results of the Taylor expansion method for the reweighting factor in Ref. [26].

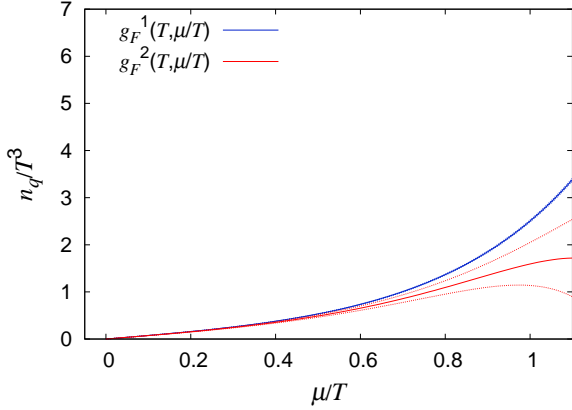


Fig. 6: μ/T dependence of n_q/T^3 at $T = 0.93T_c$. See Fig. 5 for the definition of lines. Two cases of g_F^1 and g_F^2 are plotted.

Figures 7, 8 and 9 show the μ/T dependence of n_q/T^3 at $T = 1.20T_c$, $1.35T_c$ and $2.07T_c$, respectively. Two cases of g_p^3 and g_p^5 are plotted. For each case, the solid line represents the result calculated from the mean value of $a_p^{(k)}$, whereas two dotted lines correspond to the results from the upper and lower bounds of $a_p^{(k)}$. For each temperature, the present result of g_p^3 agrees with the previous LQCD result [26] based on the Taylor expansion method for the reweighting factor, because the previous study assumes g_p^3 for n_q/T^3 . The difference between g_p^3 and g_p^5 becomes small in the range $\mu/T < 1$ as T increases. Higher-order contributions than $(\mu/T)^3$ thus become less important as T increases.

The relative difference between two results of g_p^3 and g_p^5

exceeds 10% at $\mu/T \simeq 0.72$ for $T = 1.20T_c$, 1.2 for $T = 1.35T_c$ and 2.6 for $T = 2.07T_c$. The upper bound $(\mu/T)_{\max}$ of the reliable extrapolation is plotted as a function of T/T_c in Fig. 10. The upper bound goes up as T increases, indicating that higher-order contributions than $(\mu/T)^3$ become less important. The g_p^3 extrapolation, i.e., the previous result [26] based on the Taylor expansion method for the reweighting factor thus becomes more reliable as T increases.

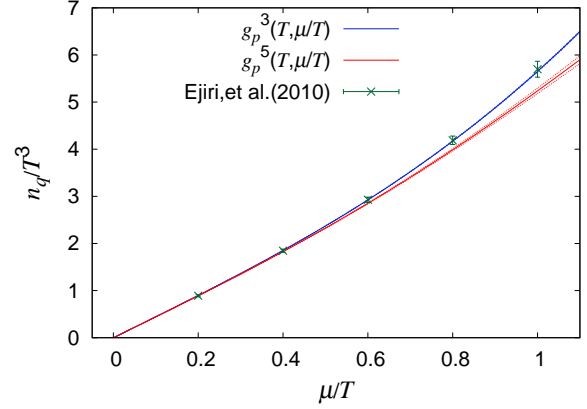


Fig. 7: μ/T dependence of n_q/T^3 at $T = 1.20T_c$. Two cases of g_p^3 and g_p^5 are plotted. For each case, the solid line stands for the result calculated from the mean value of $a_p^{(k)}$, whereas two dashed lines denote the results from the upper and lower bounds of $a_p^{(k)}$. The symbols denotes LQCD results of the Taylor expansion method for the reweighting factor in Ref. [26].

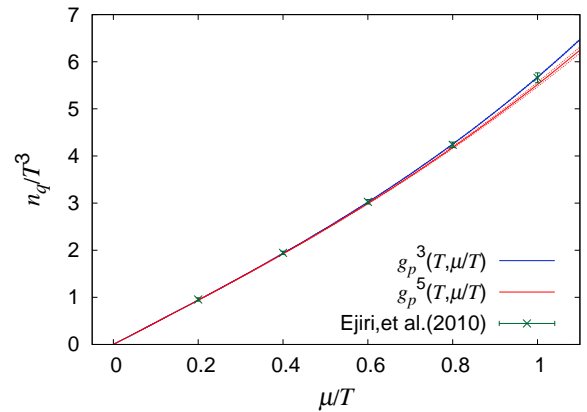


Fig. 8: μ/T dependence of n_q/T^3 at $T = 1.35T_c$. Two cases of g_p^3 and g_p^5 are plotted. See Fig. 7 for the definition of lines. The symbols denotes LQCD results of the Taylor expansion method for the reweighting factor in Ref. [26].

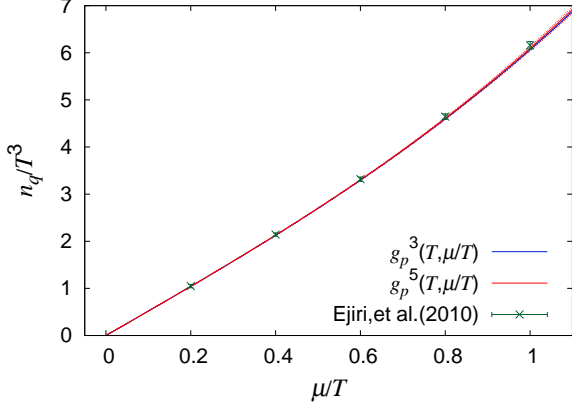


Fig. 9: μ/T dependence of n_q/T^3 at $T = 2.07T_c$. Two cases of g_p^3 and g_p^5 are plotted. See Fig. 5 for the definition of lines. The symbols denotes LQCD results of the Taylor expansion method for the reweighting factor in Ref. [26].

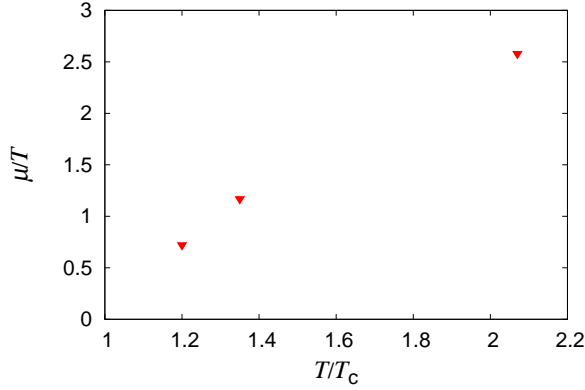


Fig. 10: T dependence of the upper bound $(\mu/T)_{\max}$ of the reliable extrapolation for the case of $T > T_{RW}$.

IV. HADRON RESONANCE GAS MODEL

Now we consider the confinement region at $T < T_c$ for the case of imaginary μ , and analyze the present LQCD results with the hadron resonance gas (HRG) model in order to understand properties of n_q and deduce the T dependence of baryon mass in the vicinity of T_c . The HRG model considers non-interacting hadrons and resonances, each classified with species i , i.e., with mass m_i , baryon number B_i and isospin I_{3i} . For the 2+1 flavor case with no μ , the HRG model well reproduces LQCD data on pressure at $T < 1.2T_c$ [29]. This means that the HRG model is applicable at $T < T_c$ and imaginary μ , because the pseudocritical temperature of deconfinement transition becomes higher as μ_I increases. The pressure

of the model is obtained by

$$p^{\text{HRG}} = -\frac{T}{V} \sum_{i \in \text{meson}} \ln Z_i^{\text{M}}(T, V, \mu_i) - \frac{T}{V} \sum_{i \in \text{baryon}} \ln Z_i^{\text{B}}(T, V, \mu_i) \quad (14)$$

with

$$\ln Z_i^{\text{M/B}} = \pm \frac{V g_i}{2\pi^2} \int_0^\infty dp p^2 \ln \left(1 \mp z_i e^{-\epsilon_i/T} \right) \quad (15)$$

for the energy $\epsilon_i = \sqrt{p^2 + m_i}$, the degeneracy factor g_i and the fugacity

$$z_i = e^{\mu_i/T} = \exp \left(\frac{B_i \mu_B + 2I_{3i} \mu_{\text{iso}}}{T} \right), \quad (16)$$

where $\mu_B (\equiv 3\mu)$ and μ_{iso} are the baryon and isospin chemical potentials, respectively. Here we consider only the case of $\mu_{\text{iso}} = 0$. The baryon number density is easily obtained as

$$n_B^{\text{HRG}} = -\frac{\partial}{\partial \mu_B} p^{\text{HRG}}. \quad (17)$$

There are lattice artifacts in LQCD simulations. These were already discussed in Refs. [25, 26, 35–37]. For small N_t , for example, thermodynamic quantities exceed the Stefan-Boltzmann (SB) limit. Since it is not easy to eliminate the lattice artifact exactly, we take the following simple prescription. We consider the lattice SB limit that is defined by the lattice action with massless and free quarks, and normalize LQCD results with the values in the lattice SB limit. We regard these normalized values as the lattice-artifact free values; see Appendix A for the quark number density in the lattice SB limit. For the HRG model, meanwhile, the quark number density is normalized by the value in the continuum SB limit. In the HRG model, we assume that nucleon mass m_N and Δ -resonance mass m_Δ depend on T only. This assumption works well in the χ^2 fitting of m_N and m_Δ to LQCD data on n_q at imaginary μ , as shown later in Fig 11. The baryon masses are determined so as to reproduce the LQCD result. Here we assume that the masses of 24 resonance states above the mass threshold m_{cut}^B are fixed at 1.8 GeV, following Ref. [35]. But the contribution of 24 states to n_q is small.

Figure 11 shows the θ dependence of the normalized quark number density n_q/n_{SB} at $T = 0.93T_c$ and $0.99T_c$. The HRG model (solid line) reproduces the θ dependence of LQCD results (symbols with error bars) for both cases of $T = 0.93T_c$ and $0.99T_c$. This means that m_N and m_Δ little depend on θ . The resulting nucleon and Δ -resonance masses are summarized in Table IV. The resulting masses are heavier than the corresponding physical values, because the quark mass is much heavier than the physical value in our simulations. As shown in Table IV, both m_N and m_Δ decrease by about 10% as T increases from $0.93T_c$ to $0.99T_c$.

Finally we consider the case of real μ . The HRG model becomes less reliable as μ/T increases, because the pseudocritical temperature of deconfinement transition goes down from

V. SUMMARY

We have investigated the μ dependence of n_q at imaginary and real μ , performing LQCD simulations at imaginary μ and extrapolating the results to the real- μ region by assuming functional forms for n_q . LQCD calculations were done on an $8^2 \times 16 \times 4$ lattice with the clover-improved two-flavor Wilson fermion action and the renormalization-group-improved Iwasaki gauge action. We considered two temperatures below T_c and four temperatures above T_c . The quark number density was computed along the line of constant physics at $m_{\text{PS}}/m_V = 0.80$.

For imaginary μ , the quark number density calculated with the Wilson-type fermion action is consistent with the previous result [28] based on the staggered-type fermion action. The LQCD results thus do not depend on the fermion action taken.

We have extrapolated n_q at imaginary μ to real μ , assuming the Fourier series g_F^n at $T < T_c$ and the polynomial series g_p^n at $T > T_{\text{RW}}$. Here the superscript n denotes the highest order taken in the partial sum. As for $T = 0.99T_c$, the present result of g_F^2 is consistent with the previous result [26] based on the Taylor expansion method for the reweighting factor in the range $\mu/T < 0.9$. The present analytic continuation based on g_F^2 is thus reliable at $\mu/T < 0.9$ for $T = 0.99T_c$. Furthermore, the difference between the two results of g_F^1 and g_F^2 reduces as T decreases from T_c , indicating that higher-order contributions become less important as T decreases. Therefore, the present extrapolation based on g_F^2 is reliable at $\mu/T < 0.9$ for any T less than T_c .

For $T > T_{\text{RW}}$, the previous study based on the Taylor expansion method for the reweighting factor has contributions up to $(\mu/T)^3$, but the present g_p^5 extrapolation retains contributions up to $(\mu/T)^5$. Using this advantage of the present method from the previous method, we have estimated to what extent the Taylor expansion or the g_p^5 extrapolation works. The upper bound $(\mu/T)_{\text{max}}$ of the reliable extrapolation goes up as T increases from T_{RW} , because higher-order contributions become less important.

The HRG model is reliable in the deconfinement region. For the 2+1 flavor case with no μ , in fact, the HRG model well reproduces LQCD data on pressure at $T < 1.2T_c$ [29]. The pseudocritical temperature of deconfinement transition goes down from $T = T_{\text{RW}}$ as $(\mu/T)^2$ increases from $-(\pi/3)^2$ to plus values. This means that the HRG model is more reliable at imaginary μ than real μ in the vicinity of T_c . Using this property, we have deduced the T dependence of m_N and m_Δ with the HRG model from the n_q calculated with LQCD simulations at imaginary μ . The HRG model well reproduces the LQCD results, when m_N and m_Δ are assumed to depend on T only. This indicates that m_N and m_Δ little depend on $\theta (= \mu_I/T)$. For the T dependence, m_N and m_Δ decrease by about 10% when T increases from $0.93T_c$ to $0.99T_c$. This is a handy way of deducing the T dependence of m_N and m_Δ in the vicinity of T_c . This method is quite practical, since it is not easy to measure the T dependence of the pole masses of nucleon and Δ -resonance directly with LQCD simulations.

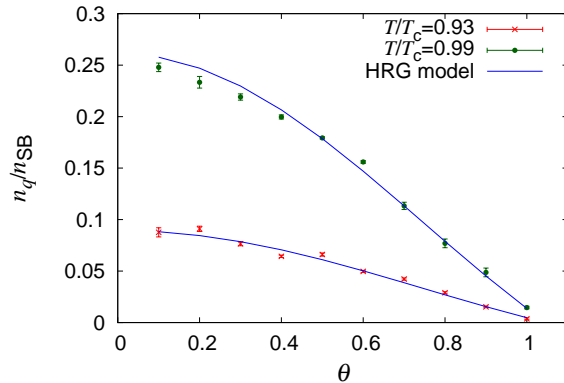


Fig. 11: θ dependence of n_q/n_{SB} at $T = 0.93T_c$ and $0.99T_c$. The cross and square symbols with error bars represent the LQCD results at $T = 0.93T_c$ and $0.99T_c$, respectively, whereas the solid lines stand for the HRG model results.

T/T_c	m_N	m_Δ
0.93	1091 MeV	1547 MeV
0.99	940 MeV	1385 MeV

TABLE IV: m_N and m_Δ at $T = 0.93T_c$ and $0.99T_c$.

T_c as μ/T increases from zero. Figure 12 shows the μ/T dependence of n_q/n_{SB} at $T = 0.99T_c$. In the range $\mu/T < 0.4$, the HRG model result (solid line) is consistent with the previous LQCD results [26] (symbols with error bars) based on the Taylor expansion method for the reweighting factor. Beyond the range, the HRG model overestimates the LQCD results. The HRG model is thus reliable only at $\mu/T < 0.4$ for the case of $T = 0.99T_c$.

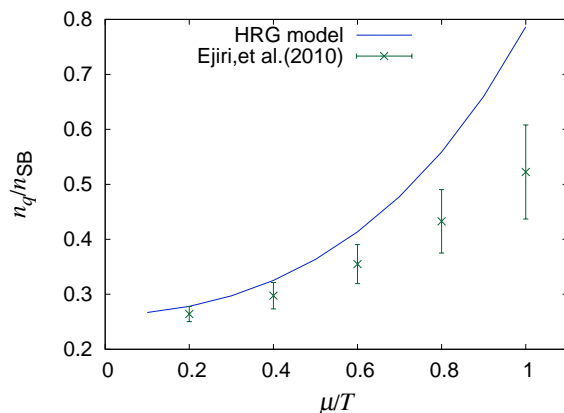


Fig. 12: μ/T dependence of n_q/n_{SB} in the real μ region for $T = 0.99T_c$. The symbols with error bars stand for LQCD results of the Taylor expansion method for the reweighting factor in Ref. [26], while the solid line is the result of the HRG model.

Acknowledgments

We thank A. Nakamura and K. Nagata for useful discussions and giving the LQCD program codes. We are also grateful to I.-O. Stamatescu, T. Sasaki and T. Saito for helpful discussions. J. T., H. K., and M. Y. are supported by Grant-in-Aid for Scientific Research (No. 26400278, No. 26400279 and No. 25-3944) from the Japan Society for the Promotion of Science (JSPS). The numerical calculations were performed on NEC SX-9 and SX-8R at CMC, Osaka University and on HITACHI HA8000 at Research Institute for Information Technology, Kyushu University.

Appendix A: Quark number density for the Wilson fermion in the massless free-gas limit

We consider n_q for the Wilson fermion in the lattice SB limit (the massless free-gas limit). In the high- T limit, we can consider a quark as a massless and non-interacting particle, since the effects of finite quark mass and interactions between quarks are negligible there. In Appendix of Ref. [26], the lattice SB limit is discussed except for the quark number density.

The partition function with free Wilson fermions is given by

$$Z(\kappa, \hat{\mu}) = (\det M)^{N_f}, \quad (\text{A1})$$

$$M_{xy} = \delta_{xy} - \kappa \sum_{i=1}^3 \left[(1 - \gamma_i) \delta_{x+\hat{i}, y} + (1 + \gamma_i) \delta_{x-\hat{i}, y} \right] - \kappa \left[e^{+\hat{\mu}} (1 - \gamma_4) \delta_{x+\hat{4}, y} + e^{-\hat{\mu}} (1 + \gamma_4) \delta_{x-\hat{4}, y} \right], \quad (\text{A2})$$

on an $N_x \times N_y \times N_z \times N_t$ lattice. After the unitary transformation to momentum space, we obtain

$$Z(1/8, \hat{\mu}) = \left(\prod_k \det \tilde{M}(k) \right)^{N_c N_f} \quad (\text{A3})$$

$$\det \tilde{M}(k) = \frac{16}{8^4} \left[\sum_i \sin^2 k_i + \left\{ 2 \sum_i \sin^2 \left(\frac{k_i}{2} \right) \right\}^2 + 4 \left\{ 2 \sum_i \sin^2 \left(\frac{k_i}{2} \right) + 1 \right\} \sin^2 \left(\frac{k_t - i\hat{\mu}}{2} \right) \right]^2 \quad (\text{A4})$$

in the massless quark limit $\kappa = 1/8$, where \tilde{M} is the fermion matrix in momentum space, and

$$k_i = \frac{2\pi j_i}{N_i}, \quad j_i = 0, \pm 1, \dots, N_i/2 \quad (\text{A5})$$

for the spatial components ($i = x, y, z$) and

$$k_t = \frac{2\pi(j_t + 1/2)}{N_t}, \quad j_t = 0, \pm 1, \dots, N_t/2 \quad (\text{A6})$$

for the time component. The quark number density in the lattice SB limit is then obtained as

$$\begin{aligned} \frac{n_q}{T^3} &= \frac{N_t^3}{N_V} \frac{\partial}{\partial \hat{\mu}} \ln Z(1/8, \hat{\mu}) \\ &= N_c N_f \frac{N_t^3}{N_V} \sum_k \frac{\partial \det \tilde{M}(k)}{\partial \hat{\mu}} \left[\det \tilde{M}(k) \right]^{-1} \end{aligned} \quad (\text{A7})$$

with

$$\begin{aligned} \frac{\partial \det \tilde{M}(k)}{\partial \hat{\mu}} &= -\frac{1}{8^2} \left\{ 2 \sum_i \sin^2 \left(\frac{k_i}{2} \right) + 1 \right\} \\ &\quad \times (\sinh \hat{\mu} \cos k_t + i \cosh \hat{\mu} \sin k_t). \end{aligned} \quad (\text{A8})$$

The quark-number density at imaginary μ is obtained by replacing $\hat{\mu}$ by $i\hat{\mu}_I$ in Eqs. (A7) and (A8).

-
- [1] P. B. Demorest, T. Pennucci, S. M. Ransom, M. S. E. Roberts, and J. W. T. Hessels, *Nature* **467**, 1081 (2010).
[2] L. Kumar (for the STAR Collaboration), *Nucl. Phys. A*, **904**, 256c, (2013).
[3] E. O'Brien (for the PHENIX Collaboration), *Nucl. Phys. A*, **904**, 264c, (2013).
[4] S. Muroya, A. Nakamura, C. Nonaka, and T. Takaishi, *Prog.*

- Theor. Phys.* **110**, 615 (2003).
[5] P. de Forcrand, *Proc. Sci., LAT2009*, **010**, arXiv:1005.0539 [hep-lat], (2009).
[6] G. Aarts, *Phys. Rev. Lett.* **102**, 131601 (2009).
[7] G. Aarts, L. Bongiovanni, E. Seiler, D. Sexty, and I. -O. Stamatescu, *Eur. Phys. J. A* **49**, 89 (2013).
[8] D. Sexty, *Phys. Lett. B* **729**, 108 (2014).

- [9] G. Aarts, E. Seiler, D. Sexty, and I. -O. Stamatescu, arXiv:1408.3770 [hep-lat], (2014).
- [10] M. Cristoforetti, F. Di. Renzo, and L. Scorzato, Phys. Rev. D **86**, 074506 (2012).
- [11] H. Fujii, D. Honda, M. Kato, Y. Kikukawa, S. Komatsu, and T. Sano, J. High Energy Phys. **10**, 147 (2013).
- [12] A. Roberge, and N. Weiss, Nucl. Phys. **B275**, 734 (1986).
- [13] Y. Aoki, G. Endrödi, Z. Fodor, S. D. Katz, and K. K. Szabó, Nature **443**, 675 (2006).
- [14] H. Kouno, Y. Sakai, K. Kashiwa and M. Yahiro, J. Phys. G **36**, 115010 (2009) [arXiv:0904.0925 [hep-ph]].
- [15] P. de Forcrand, and O. Philipsen, Nucl. Phys. **B642**, 290 (2002).
- [16] L.-K. Wu, X.-Q. Luo, and H.-S. Chen, Phys. Rev. D **76**, 034505 (2007).
- [17] M. D’Elia and M.-P. Lombardo, Phys. Rev. D **67**, 014505 (2003).
- [18] M. D’Elia and M.-P. Lombardo, Phys. Rev. D **70**, 074509 (2004).
- [19] P. de Forcrand, and O. Philipsen, Phys. Rev. Lett. **105**, 152001 (2010).
- [20] K. Nagata and A. Nakamura, Phys. Rev. D **83**, 114507 (2011).
- [21] Y. Sakai, K. Kashiwa, H. Kouno and M. Yahiro, Phys. Rev. D **77**, 051901 (2008) [arXiv:0801.0034 [hep-ph]].
- [22] Y. Sakai, T. Sasaki, H. Kouno, and M. Yahiro, J. Phys. G **39**, 035004 (2012).
- [23] Y. Sakai, K. Kashiwa, H. Kouno, M. Matsuzaki, and M. Yahiro, Phys. Rev. D **78**, 076007 (2008).
- [24] J. Sugano J. Takahashi M. Ishii H. Kouno and M. Yahiro, Phys. Rev. D **90**, 037901 (2014).
- [25] C. R. Allton, S. Ejiri, S. J. Hands, O. Kaczmarek, F. Karsch, E. Laermann, and C. Schmidt, Phys. Rev. D **68**, 014507 (2003).
- [26] S. Ejiri et al. (WHOT-QCD Collaboration), Phys. Rev. D **82**, 014508 (2010).
- [27] M. D’Elia F. D. Renzo, and M. P. Lombardo, Phys. Rev. D **76**, 114509 (2007).
- [28] M. D’Elia and F. Sanfilippo, Phys. Rev. D **80**, 014502 (2009).
- [29] S. Borsanyi, G. Endrodi, Z. Fodor, S. D. Katz, S. Krieg, C. Ratti and K. K. Szabo, JHEP **1208**, 053 (2012) [arXiv:1204.6710 [hep-lat]].
- [30] A. Ali Khan et al. (CP-PACS Collaboration), Phys. Rev. D **63**, 034502 (2000).
- [31] Y. Iwasaki, Nucl. Phys. **B258**, 141 (1985).
- [32] B. Sheikholeslami and R. Wohlert, Nucl. Phys. **B259**, 572 (1985).
- [33] A. Ali Khan et al. (CP-PACS Collaboration), Phys. Rev. D **64**, 074510 (2001).
- [34] Y. Maezawa et al. (WHOT-QCD Collaboration), Phys. Rev. D **75**, 074501 (2007).
- [35] P. Huovinen and P. Petreczky, Nucl. Phys. A **837**, 26 (2010).
- [36] O. Philipsen and L. Zeidlewicz, Phys. Rev. D **81**, 077501 (2010).
- [37] A. Bazavov et al. (HotQCD Collaboration), Phys. Rev. D **85**, 054503 (2012).